Edge states in graphene quantum dots: Fractional quantum Hall effect analogies and differences at zero magnetic field

Igor Romanovsky, Constantine Yannouleas, and Uzi Landman
School of Physics, Georgia Institute of Technology, Atlanta, Georgia 30332-0430, USA
(Received 30 October 2008; revised manuscript received 17 December 2008; published 11 February 2009)

We investigate the way that the degenerate manifold of midgap edge states in quasicircular graphene quantum dots with zigzag boundaries supports, under *free-magnetic-field* conditions, strongly correlated many-body behavior analogous to the fractional quantum Hall effect (FQHE), familiar from the case of semiconductor heterostructures in high-magnetic fields. Systematic exact-diagonalization (EXD) numerical studies are presented for $5 \leq N \leq 8$ fully spin-polarized electrons and for total angular momenta in the range of $N(N-1)/2 \leq L \leq 150$. We present a derivation of a rotating-electron-molecule (REM) type wave function based on the methodology introduced earlier [C. Yannouleas and U. Landman, Phys. Rev. B **66**, 115315 (2002)] in the context of the FQHE in two-dimensional semiconductor quantum dots. The EXD wave functions are compared with FQHE trial functions of the Laughlin, compact composite fermion, and the derived REM types. It is found that a variational extension of the REM offers a better description for all fractional fillings compared with that of the Laughlin functions (including total energies and overlaps), a fact that reflects the strong azimuthal localization of the edge electrons. In contrast with the multiring arrangements of electrons in circular semiconductor quantum dots, the graphene REMs exhibit in all instances a single $(0,N)$ polygonal-ring molecular (crystalline) structure, with all the electrons localized on the edge. Disruptions in the zigzag boundary condition along the circular edge act effectively as impurities that *pin* the electron molecule, yielding single-particle densities with broken rotational symmetry that portray directly the azimuthal localization of the edge electrons.

DOI: 10.1103/PhysRevB.79.075311 PACS number(s): 73.21.La, 73.43.Cd

I. INTRODUCTION

Since the discovery[1] of the fractional quantum Hall effect (FQHE) in two-dimensional (2D) semiconductor heterostructures in the presence of a high perpendicular magnetic field ($\mathcal{B}$), phenomena associated with strongly correlated electrons in the lowest Landau level (LLL) have attracted significant and continuous attention.[2–13] Early on, it was realized that the essential many-body physics in the LLL could be most effectively grasped through the use of trial wave functions, with celebrated examples being the Jastrow-type Laughlin[2] (JL) and composite fermion[5] (CF) trial functions associated with the formation of a special class of quantum-liquid states.[6] Later interest in finite 2D electronic systems, such as semiconductor quantum dots (QDs) under high $\mathcal{B}$, led to the consideration of a different class of analytic trial functions known as rotating-electron (or Wigner) molecules[8–11] (REMs or RWMs). An advantage of the REMs is that, while they exhibit good-total angular momenta, they directly incorporate the molecular (crystalline) configurations that dominate the anisotropic pair-correlation functions revealed through numerical exact-diagonalization (EXD) studies for a finite number of electrons under high $\mathcal{B}$ in a disk geometry. The initial derivation[8] of the REM trial functions generated a flare of theoretical activity aimed at finding which class of trial functions (or combination of them) is most appropriate for describing the correlated many-body physics in the LLL of a small number of electrons N.[7,9–13] Furthermore, experimental advances in the field of ultracold trapped neutral atoms have been followed by considerable theoretical activity regarding the nature of correlated states in the LLL that are formed during the rapid rotation of the trap (see, e.g., Refs. 14–19).

Recent progress in the fabrication of new materials, and in particular in isolating and handling of a single graphene sheet,[20–23] offers most promising materials for future, post-silicone, miniaturized electronics[24,25] (sometime called nanoelectronics). This expectation is based on the two-dimensional character of graphene, where the electrons are essentially confined in the spatial direction normal to the graphene plane. Fabrication of nanoscale device elements for use in electronics, spintronics, and information processing, such as single-electron transistors, quantum point contacts, and quantum dots, would require additional confinement in the other two spatial dimensions. However, to achieve the requested additional confinement, techniques (based on electrostatic gating) developed for the creation of QDs in semiconductors (such as GaAs) cannot be used because of the unique electronic structure of graphene. The difficulty originates from the relativistic, Dirac-type, nature of the low-energy quasiparticles in graphene. In particular, the gapless nature of the electrons in graphene[26] allows them to penetrate unimpeded through a high and wide potential barrier.[27] This phenomenon, which is known as the Klein paradox,[28,29] is in fact not a paradox but a consequence of the relativistic character of the electrons, with a sufficiently high potential being repulsive for electrons but attractive for positrons, thus resulting in positron states inside the barrier which can be matched to the electronic continuum states outside, consequently resulting in perfect transmission through the barrier; the underlying property of the Dirac equation is known as the charge-conjugation symmetry.

In light of the above, one wishes to explore alternative nonelectrostatic methods for fabrication of lower dimensionality graphene nanostructures. One route for achieving the desired added planar confinement consists of etching or cut-

ting graphene into the desired geometry (e.g., ribbons,[30–32] circular disks, or other shapes[33–35]). It is expected that further progress in fabrication, characterization, and understanding of the properties of such graphene nanostructures (in particular, zero-dimensional QDs) would lead to their use for the study of interesting many-body phenomena, as well as their employment as components in miniaturized electronic devices.

Here we explore theoretically certain properties of circular graphene quantum dots, defined via cutting the desired shape from a two-dimensional extended sheet. In particular, we regard investigations of graphene QDs as providing an opportunity for re-examination (and possibly experimental resolution) of remaining questions concerning the appropriateness of liquid-type vs molecular-type trial functions for a finite number of 2D electrons. Indeed, it has been known for some time that manifolds of degenerate midgap edge states exist in graphene nanostructures (such as graphene ribbons) when they terminate in a zigzag boundary.[36,37] In a recent paper[38] it was noted that the single-particle edge states associated with *circular* graphene dots with zigzag boundary conditions, and in the absence of an applied magnetic field, display degeneracies and quantum numbers in close analogy with the manifold of single-particle states that form the familiar LLL in semiconductor heterostructures at high $\mathcal{B}$. Furthermore, the numerical calculations in Ref. 38, covering rather limited ranges of electron numbers (i.e., $2 \leq N \leq 5$) and total angular momenta [i.e., $N(N-1) \leq L \leq 60$], suggested that the use of quantum-liquid-type trial functions in relation to the graphene-dot lowest Landau level (GD-LLL) may be less promising than that of Wigner-crystal-type *Ansätze*.

In this paper, applying a methodology based on angular-momentum projection techniques, which was introduced in Ref. 8, we derive analytic REM trial functions appropriate for the GD-LLL. By introducing a single variational parameter, we demonstrate numerically (through systematic comparisons with EXD calculations) that the variational variant of the REM (referred to as VREM) substantially outperforms the Laughlin and compact composite-fermion trial functions (as well as the *Ansatz* in Ref. 38) for all values of fractional fillings within the expanded angular-momentum range $N(N-1)/2 \leq L \leq 150$ for the following numbers of electrons $N=5$, 6, 7, and 8.

II. LOWEST LANDAU LEVEL FOR CIRCULAR GRAPHENE DOTS

A. Single-particle edge states

It is well known[39] that the low-energy-band structure of graphene can be described by a linearized tight-binding Hamiltonian H. For a graphene dot with a circular symmetry this linearized Hamiltonian is given[38] in polar coordinates by

$$H = \hbar v_F \begin{pmatrix} H_+ & 0 \\ 0 & H_- \end{pmatrix}, \tag{1}$$

where

$$H_s = \begin{pmatrix} 0 & e^{-is\phi}\left(-i\partial_r - \frac{s}{r}\partial_\phi\right) \\ e^{is\phi}\left(-i\partial_r + \frac{s}{r}\partial_\phi\right) & 0 \end{pmatrix}, \tag{2}$$

where v_F is the Fermi velocity and $s = \pm$ specifies the degenerate in energy valleys for the two bands formed at the K and K' points. The index s can be considered as a "pseudospin," which creates a fourfold degeneracy when the spin degree of freedom is also considered. The general solution of the Hamiltonian in Eq. (2) is a two component vector of the form

$$\begin{pmatrix} u_s^A(r,\phi) \\ u_s^B(r,\phi) \end{pmatrix}, \tag{3}$$

where A and B denote the two triangular sublattices of graphene.

The usual volume solutions (which are zero on the graphene boundary but otherwise extend everywhere inside the area enclosed by the graphene dot) have energy $E_k = v_F k$, with u_s^A and u_s^B components that are expressed via the Bessel functions. Here we are not interested in such volume solutions. Instead we focus on the special edge states with zero energy $E=0$. These $E=0$ states are eigenfunctions of H_s under the assumption that the graphene boundary exhibits an uninterrupted zigzag edge;[36–38] an outline of their derivation from the Hamiltonian H_s is given in Appendix A.

Henceforth we will only need to remember the precise form of the edge states, which is given by

$$\begin{pmatrix} \psi_l^{A+} \\ \psi_l^{B+} \end{pmatrix} = \begin{pmatrix} \sqrt{\frac{l+1}{\pi R^{2(l+1)}}} r^l e^{il\phi} \\ 0 \end{pmatrix} \tag{4}$$

and

$$\begin{pmatrix} \psi_l^{A-} \\ \psi_l^{B-} \end{pmatrix} = \begin{pmatrix} 0 \\ \sqrt{\frac{l+1}{\pi R^{2(l+1)}}} r^l e^{il\phi} \end{pmatrix}. \tag{5}$$

Namely, one of the A and B components is everywhere zero (both on the boundary and inside the dot) and the two valleys + and − are decoupled even when the two-body Coulomb interaction is considered (which is the main focus of this paper; see below). As a result, in the following, we will drop the sublattice and valley indices. We will also assume that the electrons are fully polarized.

Since the single-particle angular momentum $l \geq 0$ (to guarantee normalizability), the manifold of such model edge states forms a set of degenerate states similar to the LLL, familiar from the case of 2D semiconductor devices at very high-magnetic fields $\mathcal{B}$. We will call the manifold[40] of degenerate edge states with $l \geq 0$ the GD-LLL. The main difference [apart from the normalization constant, see Eq. (3) in Ref. 8] between the two cases is that the single-particle states in the usual LLL exhibit an additional Gaussian multiplicative factor $\exp(-r^2/4\Lambda_{\mathcal{B}}^2)$, where $\Lambda_B = \hbar c/(e\mathcal{B})$ is the magnetic length. This Gaussian is missing from the expression for the

edge states in Eqs. (4) and (5); instead one has $\psi_l \equiv 0$ for $r > R$. It is thus natural to investigate possible similarities related to FQHE physics.

B. Classes of variational many-body wave functions

FQHE physics in the LLL has been extensively investigated for the case of 2D semiconductor quantum dots.[7,11] A main focus has been the underlying nature of the correlated many-body states, i.e., "liquid" (Laughlin, composite fermions) or molecule ("crystalline," REM). Detailed comparisons of pair-correlation functions between JL/CF and REM states with EXD ones support the view that the molecular (localized electrons) picture in semiconductor QDs provides the most appropriate description. The emergence of a GD-LLL, as described above in graphene dots, offers a further area for testing the appropriateness of liquid-type variational wave functions (JL/CF) versus those that describe REMs. First we will proceed with deriving a modified REM trial wave function that takes into consideration the differences between the single-particle states which span the usual LLL (zero-node 2D-harmonic-oscillator states) and the GD-LLL (edge states).

III. DERIVATION OF VARIATIONAL REM TRIAL WAVE FUNCTIONS FOR GRAPHENE DOTS

A. Intermediary parameter-free REM functions

REM analytical wave functions in the LLL for electrons in two-dimensional semiconductor quantum dots were derived earlier in Ref. 8. The physics underlying such a derivation is based on the theory of symmetry breaking at the mean-field level and of subsequent symmetry restoration via projection techniques.[11,41] In particular, this approach consists of two steps:

(I) At the *first step*, one constructs a Slater determinant $\Psi^N(z_1,\ldots,z_N)$ out of displaced single-particle states $u(z_j,Z_{0,j})$, $j=1,\ldots,N$, which represent the electrons localized at the positions $Z_{0,j}$, with (omitting the particle indices) $z=x+iy=re^{i\phi}$ and $Z_0=X_0+iY_0=R_0e^{i\phi_0}$. Note that necessarily all electrons are localized radially on the edge of the graphene dot, so that $R_0=R$.

Naturally, for the LLL case of semiconductor QDs, the localized $u(z,Z_0)$ single-particle states (referred to also as orbitals) were taken to be displaced Gaussians with appropriate Peierls phases due to the presence of a perpendicular magnetic field [see Eq. (1) in Ref. 8]. In the case of electrons in graphene dots, however, the GD-LLL is spanned by edge-like orbitals (without a Gaussian factor), i.e.,

$$\psi_l(z) = \sqrt{\frac{l+1}{\pi R^2}}\frac{z^l}{R^l}, \tag{6}$$

and as a result the appropriate localized orbitals are taken to have an exponential form

$$u(z,Z_0) = G\exp(z/Z_0), \tag{7}$$

with G being the normalization constant (depending only on R). The fact that $u(z,Z_0)$ in Eq. (7) represents a localized electron is illustrated in Fig. 1.

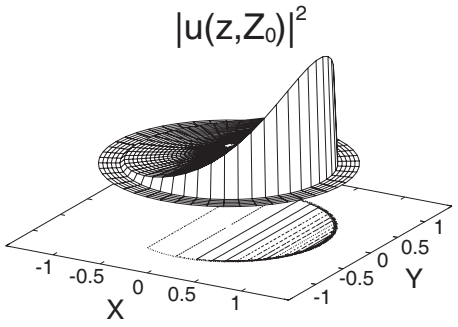

FIG. 1. The displaced orbital $u(z,Z_0)$ (modulus square) representing a localized electron at the point $Z_0=1+0i$. The radius R of the dot serves as the unit of length.

The localized orbital can be expanded in a series over the basis functions in Eq. (6) in the following way:

$$u(z,Z_0) = \sum_{l=0}^{\infty} C_l(Z_0)\psi_l(z), \tag{8}$$

with

$$C_l(Z_0) = G\frac{\sqrt{\pi}R^{l+1}}{l!\sqrt{l+1}}\frac{1}{Z_0^l}. \tag{9}$$

When constructing the many-body Slater determinant $\Psi^N[z]$, one considers N orbitals $u(z_j,Z_{0,j})$ representing N electrons on a ring of radius R (the radius of the graphene dot) forming a regular polygon, i.e.,

$$Z_{0,j} = Re^{2\pi i(1-j)/N}, \quad 1 \le j \le N. \tag{10}$$

The single Slater determinant $\Psi^N[z]$ represents a *static* electron (or Wigner) molecule (REM or RWM). Using Eq. (8), one finds the following expansion (within a proportionality constant):

$$\Psi^N[z] = \sum_{l_1,\ldots,l_N=0}^{\infty} \frac{\sqrt{(l_1+1)\cdots(l_N+1)}}{R^{l_1+\cdots+l_N}} C_{l_1}(Z_{0,1})\cdots C_{l_N}(Z_{0,N}) \times D(l_1,l_2,\ldots,l_N), \tag{11}$$

where $D(l_1,l_2,\ldots,l_N) \equiv \det[z_1^{l_1}, z_2^{l_2}, \ldots, z_N^{l_N}]$; the elements of the determinant are the functions $z_i^{l_j}$, with $z_1^{l_1}, z_2^{l_2}, \ldots, z_N^{l_N}$ being the diagonal elements.

(II) At the *second step*, the Slater determinant $\Psi^N[z]$ breaks the rotational symmetry and thus it is not an eigenstate of the total angular momentum $\hbar\hat{L}=\hbar\Sigma_{j=1}^N \hat{l}_j$. However, one can restore[8,11] the rotational symmetry by applying onto $\Psi^N[z]$ the projection operator

$$\mathcal{P}_L \equiv \frac{1}{2\pi}\int_0^{2\pi} d\gamma e^{i\gamma(\hat{L}-L)}, \tag{12}$$

where $\hbar L$ are the eigenvalues of the total angular momentum.

When applied onto $\Psi^N[z]$, the projection operator $\mathcal{P}_L$ acts as a Kronecker delta: from the unrestricted sum in Eq. (11) it picks up only those terms having a given total angular mo-

mentum L (henceforth we drop the constant prefactor $\hbar$ when referring to angular momenta). As a result the projected wave function $\Phi_L^N = \mathcal{P}_L \Psi^N$ is written as (within a proportionality constant)

$$\Phi_L^N[z] = \sum_{l_1,\ldots,l_N}^{l_1+\cdots+l_N=L} \frac{D(l_1,\ldots,l_N)}{l_1!\ldots l_N!} e^{i(\phi_1^0 l_1+\cdots+\phi_N^0 l_N)}, \quad (13)$$

with $\phi_j^0 = 2\pi(j-1)/N$.

We further observe that it is advantageous to rewrite Eq. (13) by restricting the summation to the ordered arrangements $l_1 < l_2 < \cdots < l_N$, in which case we get

$$\Phi_L^N[z] = \sum_{0\le l_1<l_2<\cdots<l_N}^{l_1+l_2+\cdots+l_N=L} \frac{D(l_1,\ldots,l_N)}{l_1!\ldots l_N!} \times \det[e^{i\phi_1^0 l_1}, e^{i\phi_2^0 l_2}, \ldots, e^{i\phi_N^0 l_N}]. \quad (14)$$

The second determinant in Eq. (14) can be shown[42] to be equal (within a proportionality constant) to the following product of sine terms times a phase factor (independent of the individual l_j's):

$$e^{i\pi(N-1)L/N} \prod_{1\le j<k\le N} \sin\left[\frac{\pi}{N}(l_j - l_k)\right]. \quad (15)$$

Thus, the final result for the REM wave function is (within a proportionality constant)

$$\Phi_{N,L}^{\mathrm{REM}}[z] = \sum_{0\le l_1<l_2<\cdots<l_N}^{l_1+l_2+\cdots+l_N=L} \frac{D(l_1,l_2,\ldots,l_N)}{l_1!\,l_2!\ldots l_N!} \times \prod_{1\le j<k\le N} \sin\left[\frac{\pi}{N}(l_j - l_k)\right]. \quad (16)$$

B. Introducing the variational parameter

As will be described below, we found that the agreement between the REM in graphene dots and the EXD solutions can be improved in a nontrivial way by introducing variational parameters. In particular, we found that consideration of a single variational parameter α serves our purpose remarkably well. Specifically, one replaces the prefactor

$$\frac{1}{l_1!\,l_2!\ldots l_N!} \quad (17)$$

in Eq. (16) by the following expression:

$$\frac{[(l_1+1)(l_2+1)\cdots(l_N+1)]^{(1-\alpha)/2}}{(l_1!\,l_2!\ldots l_N!)^{\alpha}}. \quad (18)$$

We call the α-optimized wave functions the *variational* REM functions (denoted by VREM). When $\alpha=1$, the VREM coincides with the parameter-free REM expression. We note that a single-parameter variational crystal-type wave function, but with a different dependence on the parameter α, has also been employed in Ref. 38. The present choice of variational parameter [see Eq. (18)] produces substantially better results (see below). From a practical point of view, we note that the crystal-type wave function proposed in Ref. 38 does not contain a "less-than" ordered-arrangement restriction in the summation indices $l_1,\ldots,l_N$, and as a consequence it generates an exponentially larger number of expansion terms, thus greatly inhibiting numerical evaluations for larger N and L.

IV. EXACT DIAGONALIZATION AND TWO-BODY COULOMB MATRIX ELEMENTS

For a circular graphene QD comprising N electrons in the GD-LLL, the many-body Hamiltonian $\mathcal{H}$ comprises only the two-particle interelectron Coulomb repulsion, i.e.,

$$\mathcal{H} = \sum_{i=1}^{N}\sum_{j>i}^{N} \frac{e^2}{\kappa r_{ij}}, \quad (19)$$

where κ is the dielectric constant and r_{ij} denotes the relative distance between the i and j electrons.

The REM wave functions $\Phi_{N,L}^{\mathrm{REM}}$ derived in Sec. III will be compared to the EXD ones $\Phi_{N,L}^{\mathrm{EXD}}$ that are solutions of the exact diagonalization of Hamiltonian (19) in the many-body Hilbert space spanned by the Slater determinants,

$$\Psi_L^I[z] = \frac{1}{\sqrt{N!}} \begin{vmatrix} \psi_{l_1}(z_1) & \ldots & \psi_{l_N}(z_1) \\ \vdots & \ddots & \vdots \\ \psi_{l_1}(z_N) & \ldots & \psi_{l_N}(z_N) \end{vmatrix}, \quad (20)$$

where the single-particle functions $\psi_l(z)$ are given by the edge states of Eq. (6) and the index I counts the arrangements $0 \le l_1 < l_2 < \cdots < l_N$ with $l_1+l_2+\cdots+l_N=L$.

Namely, $\Phi_{N,L}^{\mathrm{EXD}}$ is written as

$$\Phi_{N,L}^{\mathrm{EXD}}[z] = \sum_I C_L^I \Psi_L^I[z], \quad (21)$$

and the exact diagonalization of the many-body Schrödinger equation,

$$\mathcal{H}\Phi_{N,L}^{\mathrm{EXD}}[z] = E_{N,L}^{\mathrm{EXD}} \Phi_{N,L}^{\mathrm{EXD}}[z], \quad (22)$$

yields the coefficients C_L^I and the EXD eigenenergies $E_{N,L}^{\mathrm{EXD}}$.

The matrix elements $\langle \Psi_L^I | \mathcal{H} | \Psi_L^J \rangle$ between the basis determinants [see Eq. (20)] are calculated using the Slater rules[43] and taking into account that, in the GD-LLL, the many-body Hamiltonian has contributions from the Coulomb interaction only, i.e.,

$$\mathcal{H} = \sum_{i<j} \frac{e^2}{|z_i - z_j|}. \quad (23)$$

Naturally, one also needs the two-body matrix elements of the Coulomb interaction in the basis formed out of the single-particle edge states. These matrix elements are given through appropriate analytic expressions. Indeed by defining

$$M(m,n,k) = \int dz_1 \int dz_2 \psi_{m+k}^{\dagger}(z_1)\psi_{n-k}^{\dagger}(z_2)\frac{1}{|z_1 - z_2|}\psi_m(z_1)\psi_n(z_2), \quad (24)$$

one finds

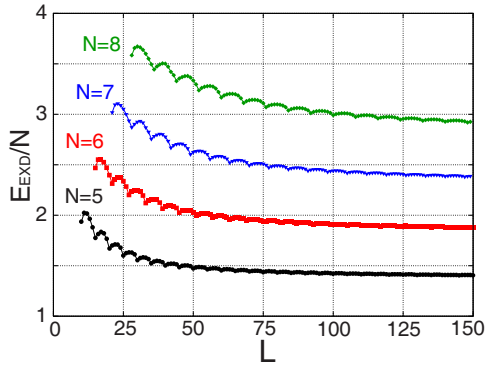

FIG. 2. (Color online) Exact diagonalization ground-state energies in the graphene-dot LLL for $N=5$, 6, 7, and 8 electrons as a function of the total angular momentum L. Observe the appearance of cusp states of enhanced stability at the magic angular momenta $L_m=N(N-1)/2+kN$, $k=0,1,2,\ldots$, a fact that indicates formation of Wigner molecules having a single polygonal-ring configuration $(0,N)$. Energies in units of $e^2/(\kappa R)$, with κ being the graphene dielectric constant and R the radius of the quantum dot. For $L\rightarrow\infty$, the ground-state energies approach asymptotically the classical electrostatic energy [see Eq. (27)].

$$M(m,n,k) = \frac{1}{R}\frac{2\pi\mathcal{C}\sqrt{\pi}}{(2m+2n+3)}\frac{\Gamma\left(k+\frac{1}{2}\right)}{\Gamma(k+1)} \times\left[\frac{\Gamma(n+1)}{\Gamma(n+2)}{}_3F_2\left(\begin{matrix}1/2, & k+1/2, & n+1; & 1\\ & k+1, & n+2 & \end{matrix}\right) + \frac{\Gamma(m+k+1)}{\Gamma(m+k+2)}{}_3F_2\left(\begin{matrix}1/2, & k+1/2, & m+k+1; & 1\\ & k+1, & m+k+2 & \end{matrix}\right)\right], \tag{25}$$

where ${}_3F_2$ is the generalized hypergeometric function[44] at the point $x=1$, Γ is the Gamma function, and

$$\mathcal{C}=\frac{\sqrt{(m+k+1)(n-k+1)(m+1)(n+1)}}{\pi^2}. \tag{26}$$

V. NUMERICAL RESULTS

A. EXD total energies

In Fig. 2 we display systematic EXD total energies in the range of $N=5$ to $N=8$ edge electrons as a function of the total angular momenta L (in the large range $0\leq L\leq 150$). This large L range and the consideration of $N>5$ electrons were not reached in another recent publication;[38] they are, however, essential for unequivocally establishing the proper similarities and differences with the high-magnetic-field physics of semiconductor QDs.

For fully polarized spins considered here, the minimum total angular momentum is $L_0=N(N-1)/2$, in analogy with the case of semiconductor QDs.[11] Furthermore, in analogy again with the case of semiconductor QDs, the total energies decrease in the average as L increases. On top of this average trend, one observes prominent oscillations of period N. These oscillations reveal that the states with $L=L_0+kN$, $k=0,1,\ldots$, are energetically the most stable in their immediate neighborhood. Borrowing the terminology from the literature[11,45] of semiconductor QDs, we refer to these states in graphene QDs as *cusp* states and the corresponding total angular momenta (i.e., $L=L_0+kN$) as *magic angular momenta*. It is well known that cusp states develop to FQHE states in the thermodynamic limit $(N\rightarrow\infty)$, with the corresponding fractional filling factor being $\nu=L_0/L$.

Following a similar analysis[11,45] with the case of semiconductor QDs, one can conclude that the appearance of the oscillatory period N in the total energies (associated with the cusp states) is a reflection of formation of $(0,N)$-type Wigner molecules, with all the electrons localized on a single ring (of radius R) at the apices of a regular N polygon. There is a major difference, however, between the present system and the semiconductor quantum dot case. That is, in semiconductor QDs, more than one isomer may form with concentric multiring arrangements occurring for $N>5$ electrons in the dot; such arrangements are denoted as $(n_1,n_2,\ldots,n_q)$ (see Ref. 11), where n_r, $r=1,2,\ldots,q$ are the number of localized electrons on each ring; $\Sigma_{r=1}^{q}n_r=N$. In contrast, in the case of graphene dots only the one-ring $(0,N)$ molecular configuration arises (with no electron residing at the geometrical center of the graphene QD).

For $L\rightarrow\infty$, the EXD energies in Fig. 2 approach the limiting value corresponding to the classical electrostatic energy of N pointlike electrons in a $(0,N)$ configuration with radius R, i.e.,

$$E^{\mathrm{cl}}(N)=\frac{e^2}{4\kappa R}NS_N, \tag{27}$$

with $S_N=\Sigma_{j=2}^{N}\{\sin[(j-1)\pi/N]\}^{-1}$.

B. EXD densities and pair correlations

The EXD eigenfunctions conserve the total angular momentum and the corresponding electron densities are circularly symmetric. This property "conceals" the presence of the Wigner molecule. The crystalline structure, however, is present in the *intrinsic* frame of reference of the electron molecule, and it can be revealed through the use of the fully anisotropic pair-correlation function $P(z,z_0)$, defined as

$$P(z,z_0)=\langle\Phi_{N,L}^{\mathrm{EXD}}|\sum_{i\neq j}\delta(z-z_i)\delta(z_0-z_j)|\Phi_{N,L}^{\mathrm{EXD}}\rangle. \tag{28}$$

$P(z,z_0)$ is often referred to as the conditional probability distribution (CPD) since it is proportional to the probability of finding an electron at z under the condition that another one is situated at the point z_0 (the so-called fixed or observation point).

In Fig. 3 we display the conditional probability distribution for the case of $N=7$ electrons and the magic total angular momentum $L=63$ $(L-L_0=7k$, with $k=6)$, which corresponds to the celebrated $\nu=1/3$ fractional filling. One clearly observes six humps (arranged in a single-ring configuration) associated with formation of a (0,7) rotating Wigner molecule. (As is well known from the literature of semiconduc-

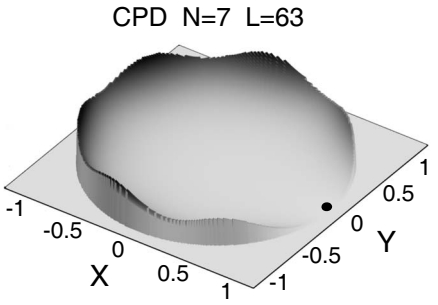

FIG. 3. Conditional probability distribution [see Eq. (28)] associated with the EXD ground state in the GD-LLL of $N=7$ electrons and for $L=63$ (corresponding to fractional filling $\nu=1/3$). One clearly observes six humps in agreement with formation of a (0,7) Wigner molecule and in contrast to the liquidlike Laughlin physical picture. The fixed (observation) point is denoted by a solid dot. Lengths in units of the graphene-dot radius R. Vertical axis in arbitrary units.

tor quantum dots,[11] the localized electron at the fixed point does not contribute any hump in the CPDs.) Similar CPDs are found for other values of N.

C. Comparison between VREM and EXD wave functions

We turn now to comparisons between the EXD wave functions and the VREM ones. We first observe that the REM and VREM functions (see Sec. III) correspond to the magic angular momenta $L=L_0+kN$, $k=0,1,2,\ldots$, since all the sine-product coefficients in expansion (16) are identically zero for $L\neq L_0+kN$. In this section, we will show that the VREM functions represent a high-quality approximation to the EXD eigenfunctions by investigating wave function overlaps and relative errors between the total energies obtained by the two methods; the relative errors are defined as $\Delta_{\mathrm{VREM}}(N,L)=(E_{N,L}^{\mathrm{VREM}}-E_{N,L}^{\mathrm{EXD}})/E_{N,L}^{\mathrm{EXD}}$.

We start by displaying in Fig. 4 the relative error $\Delta_{\mathrm{VREM}}(N,L)$ of the VREM total energies. The VREM offers an excellent approximation since the maximum relative error is less than 0.045%. For all sizes examined, the maximum relative error occurs about $\nu=1/3$ (see Sec. V A), and subsequently it decreases as L increases, approaching zero as $L\to\infty$.

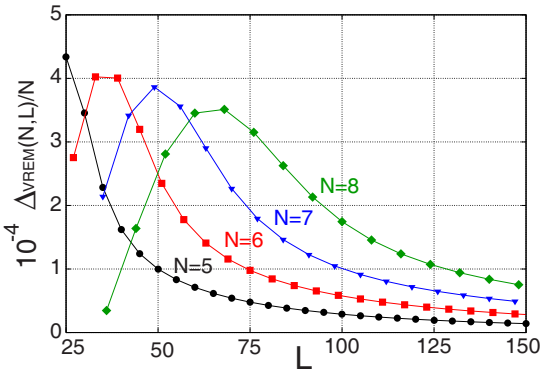

FIG. 4. (Color online) Relative error (per electron) of the VREM ground-state energies as a function of the total angular momentum L.

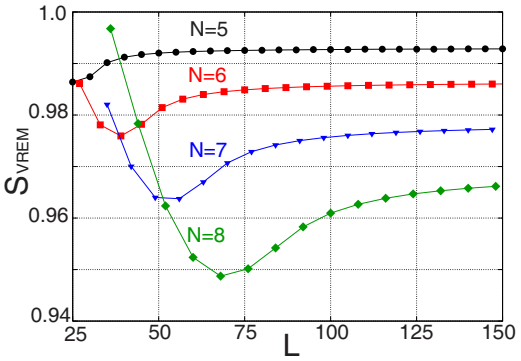

FIG. 5. (Color online) Overlaps of the VREM ground states with the EXD ones as a function of the total angular momentum L.

In Fig. 5, we display the overlaps $\mathcal{S}_{\mathrm{VREM}}\equiv\langle\Phi_{N,L}^{\mathrm{EXD}}|\Phi_{N,L}^{\mathrm{VREM}}\rangle$ between the VREM functions and the EXD solutions. These overlaps are larger than 0.985 for $N=5$ and larger than 0.95 for $N=8$ and they tend to slowly approach unity as L increases.

In Fig. 6, we display the values of the variational parameter α that optimize the VREM trial functions for a given number of electrons N as a function of L. These values are significantly different from unity (which corresponds to the parameter-free REM). In fact, the optimal α values are smaller than 0.4 and they slowly decrease to about 0.16 for $L=150$ for all the values $5\leq N\leq 8$. We stress that optimization of α is essential for achieving a high-quality reproduction of the EXD ground states. Without the additional optimization (i.e., taking only the value $\alpha=1$) the behavior of the overlaps is unsatisfactory since they tend to diminish as L increases (see Appendix B). The degradation of the overlaps of the parameter-free REM ($\alpha=1$) as L increases in the case of the graphene quantum dot contrasts with the opposite behavior of the overlaps of the parameter-free REM in the case of semiconductor quantum dots.[8,9,11] This difference is attributed to the absence of translational invariance for the electrons in the graphene quantum dot, which leads to differences in the organization of the EXD excitation spectra.

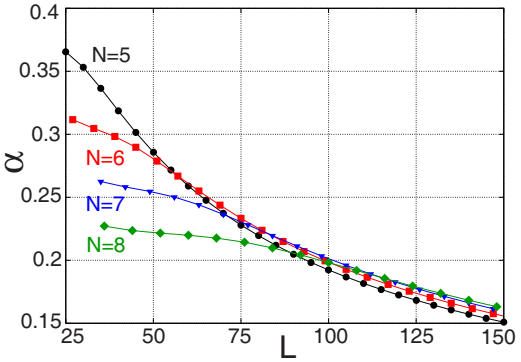

FIG. 6. (Color online) The values of the variational parameter α [see Eq. (18)] that optimize the VREM trial functions for a given N as a function of L.

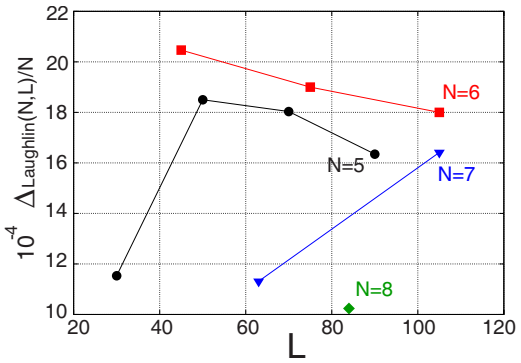

FIG. 7. (Color online) Relative error (per electron) of the Laughlin energies as a function of the total angular momentum L.

D. EXD versus Laughlin wave functions

It is interesting to compare the accuracy with which the VREM wave functions approximate the EXD ones with that of the Laughlin trial functions. The Laughlin wave functions are restricted to the so-called main (odd) fractions $\nu=1/(2m+1)$ and have played an important role in the FQHE literature of the extended two-dimensional electron gas in semiconductor heterostructures. Their form is

$$\Phi_{N,L}^{\text{Laughlin}}[z] = \prod_{1\le i<j\le N} (z_i - z_j)^{2m+1}, \tag{29}$$

where the Gaussian factors are missing (see Sec. II A) due to the differences in the single-particle states between semiconductor and graphene quantum dots; $m=0,1,2,\ldots$.

In Fig. 7, we display the relative error, $\Delta_{\text{Laughlin}}(N,L) = (E_{N,L}^{\text{Laughlin}} - E_{N,L}^{\text{EXD}})/E_{N,L}^{\text{EXD}}$, of the Laughlin total energies with respect to the ground-state EXD ones as a function of increasing total angular momentum L. The Laughlin relative errors are substantially larger (on the average by a factor of 5) than the VREM ones (see Fig. 4); this is the case even for the celebrated $\nu=1/3$ fractional filling.

In addition, the Laughlin overlaps $\mathcal{S}_{\text{Laughlin}} \equiv \langle \Phi_{N,L}^{\text{EXD}} | \Phi_{N,L}^{\text{Laughlin}} \rangle$ (plotted in Fig. 8) exhibit an unsatisfactory performance compared to that of the VREM overlaps, that is, (i) they become steadily smaller as the angular momentum increases and (ii) even for $\nu=1/3$, they are smaller than the corresponding VREM overlaps in all instances studied here, i.e., $N=5-8$ electrons in the graphene dot. We conclude that the Laughlin functions fail to capture the case of the GD-LLL, while the VREM functions offer an appropriate approximation for graphene QDs.

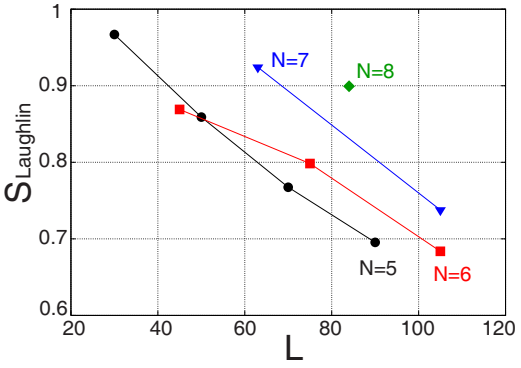

FIG. 8. (Color online) Overlaps of the Laughlin trial states with the EXD ones as a function of total angular momentum L.

E. EXD versus composite-fermion wave functions

It is also interesting to compare the accuracy with which the VREM wave functions approximate the EXD ones with that of the composite-fermion trial functions, which are more general than the Laughlin functions. Along with the Laughlin functions, the CF trial functions have played a significant role in the FQHE literature of the extended two-dimensional electron gas in semiconductor heterostructures. Their form[5,7] in the disk geometry (case of 2D QD studied here) is given by the expression

$$\Phi_L^{\text{CF}}(N) = \mathcal{P}_{\text{LLL}} \prod_{1\le i<j\le N} (z_i - z_j)^{2m} \Psi_{L^*}^{\text{IPM}}, \tag{30}$$

where $z=x+iy$ and $\Psi_{L^*}^{\text{IPM}}$ is the Slater determinant of N *noninteracting* electrons of total angular momentum L^*; it is constructed according to the independent-particle model (IPM) from the Darwin-Fock[46] orbitals $\psi_{p,l}^{\text{DF}}(z)$, where p and l are the number of nodes and the angular momentum, respectively [for the values of p and l in the nth Landau level in high $\mathcal{B}$, see Appendix F].

The single-particle electronic orbitals in the Slater determinant $\Psi_{L^*}^{\text{IPM}}$ are not restricted to the lowest Landau level. As a result, it is necessary to apply a projection operator $\mathcal{P}_{\text{LLL}}$ to guarantee that the CF wave function lies in the LLL, as appropriate for $B\to\infty$. We carry the $\mathcal{P}_{\text{LLL}}$ projection according to Sec. 4.3 of Ref. 47. After obtaining the projected CF function in the LLL, the corresponding trial function in the GD-LLL is constructed by simply replacing $\psi_{0,l}^{\text{DF}}(z)$ by the $\psi_l(z)$ in Eq. (6).

Since the CF wave function is an homogeneous polynomial in the electronic positions z_j's, its angular momentum L is related to the noninteracting total angular momentum L^* as follows:

$$L = L^* + mN(N-1) = 2mL_0. \tag{31}$$

Here we will consider the mean-field version of the composite-fermion theory, according to which the Slater determinants $\Psi_{L^*}^{\text{IPM}}$ are the so-called compact states (see Appendix F for details; the corresponding values of L^* are listed in Table II). We note that recently several extensions of the CF theory have been formulated[48] that account for residual-interaction effects among the individual $\Phi_L^{\text{CF}}(N)$ composite-fermion states. Consideration of such residual-interaction effects is beyond the scope of the present paper.

In Table I, we compare total CF and EXD energies (per particle) for $N=6$ electrons in a graphene dot. We also display the corresponding relative errors $\Delta_{\text{CF}}(N,L)/N = (E_{N,L}^{\text{CF}} - E_{N,L}^{\text{EXD}})/(NE_{N,L}^{\text{EXD}})$ and overlaps $\mathcal{S}_{\text{CF}} \equiv \langle \Phi_{N,L}^{\text{EXD}} | \Phi_{N,L}^{\text{CF}} \rangle$.

In addition to the $L=15+6k$, $k=0,1,2,\ldots$ magic angular momenta for $N=6$ found from EXD calculations (see Fig. 2), the compact-state CF theory mistakenly predicts the existence of magic angular momenta with $L=15+5k$, k

TABLE I. Total CF and EXD energies [per particle, in units of $e^2/(\kappa R)$] for $N=6$ electrons in a graphene dot. The corresponding relative errors, Δ_{CF}/N, and overlaps, $\mathcal{S}_{CF}$, are also listed. For the determination of the auxiliary angular momenta L^*, see Appendix F.

$L(L^*)$	E^{EXD}/N	E^{CF}/N	$10^{-4}\Delta_{CF}/N$	$\mathcal{S}_{CF}$
21(−9)	2.31357	2.3548	29.67	0.887
51(−9)	1.99693	2.0385	34.67	0.793
30(0)	2.24863	2.3473	73.17	0.369
60(0)	1.99452	2.0520	48.00	0.507
35(5)	2.15628	2.3022	112.8	0.356
65(5)	1.97413	2.0410	56.50	0.451
39(9)	2.06465	2.0952	24.67	0.892
69(9)	1.94477	1.9713	22.67	0.754

$=0,1,2,\ldots$, e.g., for $L=30$, 35, 60, and 65. Furthermore, even for the states with $L=15+6k$, e.g., $L=21$, 39, 51, and 69 (Table I), the quantitative performance of the compact CF functions (concerning relative errors and overlaps) is rather weak compared to that of the VREM: the CF relative errors are larger roughly by a factor of 10, while the CF overlaps are systematically smaller (<0.9) than the VREM ones (>0.97) (see Figs. 2 and 5 and Table I). As was the case with the Laughlin functions, we conclude that the compact CF functions are also at a disadvantage compared to the VREM concerning the description of strongly correlated states in the GD-LLL.

F. Comparison with the Wigner-crystal *Ansatz* in Ref. 38

Here we compare the VREM total energies with those associated with the Wigner-crystal trial function in Ref. 38 given by

$$\Phi^{WC}_{N,L}[z] = \sum_{l_1,l_2,\ldots,l_N}^{l_1+l_2+\cdots+l_N=L} \exp\left(-i\sum_n \frac{2\pi n l_n}{N}\right) \times \prod_n (l_n+1)^{w+1/2} D(l_1,l_2,\ldots,l_N), \quad (32)$$

where w is a variational parameter. In Fig. 9, we display the relative errors $\Delta_{WC}(N,L)=(E^{WC}_{N,L}-E^{EXD}_{N,L})/E^{EXD}_{N,L}$ of the WC-*Ansatz* energies relative to the EXD ones. From a comparison of these results with those displayed in Fig. 4, we conclude that the relative errors of the WC *Ansatz* are on the average at least twice as large as those corresponding to the VREM, reflecting the superior description of the GD-LLL provided by the latter function.

VI. PINNED ELECTRON MOLECULES

The zigzag geometry [on which the boundary conditions are applied (see Sec. II A)] does not allow formation of a continuous circular edge without some structural or chemical modification of the graphene hexagonal lattice structure. Without such modification, regions along the circular edge satisfying a zigzag condition must necessarily be disrupted by a number of discrete points associated with arm-chaired

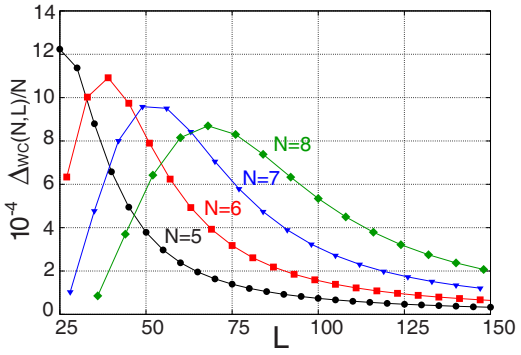

FIG. 9. (Color online) Relative errors (per electron) of the energies of the WC-*Ansatz* [Eq. (32)] as a function of total angular momentum L.

conditions.[49] It has been found that the edge states are robust in this case,[37,49] and as a result these discrete sets of disruptions act as effective impurities that modify the many-body Hamiltonian in Eq. (19). The presence of such impurity terms in the many-body Hamiltonian will mix the good-total-angular-momentum REM states, resulting in the formation of *pinned* electron molecules (PEMs). In contrast to the REMs (whose electron density is uniform along the azimuthal direction, that is, not showing any azimuthal density modulation), the electron density of a pinned electron molecule is expected not to have circular symmetry; it will exhibit angular density oscillations, and the number of humps will equal the number of electrons N.

We demonstrate this property of a PEM for two particular cases displayed in Figs. 10 and 11. Figure 10 displays for $N=7$ the electron density for the linear superposition of two REM states with $L=35$ and $L=42$, while Fig. 11 displays for $N=8$ the electron density for the linear superposition of two REM states with $L=44$ and $L=52$. In both cases the expected angular modulation is clearly well formed with seven humps in the former and eight humps in the latter case.

VII. SUMMARY

The manifold of degenerate midgap (zero-energy) edge states in circular graphene quantum dots with zigzag boundaries resembles, *under free-field conditions*,[50] the celebrated lowest Landau level, familiar from the case of semiconductor heterostructures in high-magnetic fields. The effect of *e-e* interactions in this graphene-LLL was systematically investigated and was found to generate many-body strongly correlated behavior that exhibits many similarities with the fractional quantum Hall effect.

Numerical exact-diagonalization studies were presented for $5\leq N\leq 8$ fully spin-polarized electrons and for total angular momenta in the range of $N(N-1)/2\leq L\leq 150$. Moreover, we presented a derivation of a rotating-electron-molecule type wave function based on the methodology introduced earlier[8] in the context of the FQHE in two-dimensional semiconductor quantum dots. The EXD wave functions were compared with the derived rotating-electron molecule and other suggested FQHE trial functions, such as the Laughlin function, the compact composite fermions, and

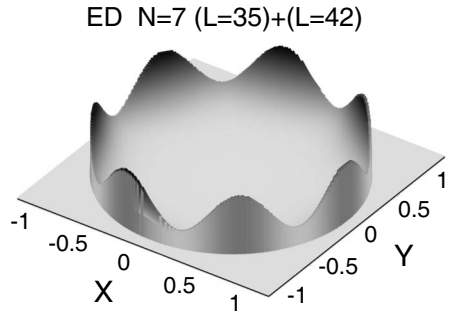

FIG. 10. Electron density of a pinned molecule for $N=7$ electrons formed from the linear superposition of two REM states with $L=35$ and $L=42$. Lengths in units of the graphene-dot radius R. Electron density in units of R^{-2}.

the Wigner-crystal *Ansatz* in Ref. 38. It was found that a variational extension of the REM offers a better description for all fractional fillings compared with that of the Laughlin, compact composite fermions, and Wigner-crystal *Ansatz* functions (including total energies and overlaps). The success of the REM function reflects the importance of strong azimuthal localization of the edge electrons in graphene quantum dots.

The variational REM functions were derived through the use of a two-step method: (i) first a mean-field-type single Slater determinant constructed out of N localized electron orbitals (that break circular symmetry) was considered; this determinant describes the finite analog of a classical static Wigner crystal and (ii) a multideterminantal wave function was generated through the subsequent application of projection techniques that introduced azimuthal fluctuations and restored the circular symmetry and good-total angular momenta.

In contrast with the multiring arrangements of electrons in circular semiconductor quantum dots, we found that the graphene REMs exhibited in all instances a single $(0,N)$ polygonal-ring molecular structure. Disruptions in the zigzag boundary condition along the circular edge behave effectively as crystal-field effects that *pin* the electron molecule, yielding single-particle densities with broken rotational symmetry that portray directly the azimuthal localization of the edge electrons.

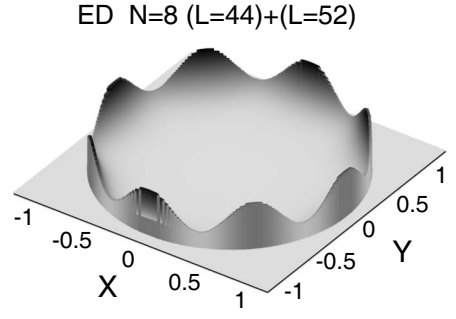

FIG. 11. Electron density of a pinned molecule for $N=8$ electrons formed from the linear superposition of two REM states with $L=44$ and $L=52$. Lengths in units of the graphene-dot radius R. Electron density in units of R^{-2}.

ACKNOWLEDGMENT

This work was supported by the U.S. DOE (Grant No. FG05-86ER45234).

APPENDIX A: MORE ON EDGE STATES

The general solution of the eigenvalue equation corresponding to the linearized tight-binding Hamiltonian (2) is of the form

$$\begin{pmatrix} \psi_l^{As} \\ \psi_l^{Bs} \end{pmatrix} = \begin{pmatrix} \chi_l^{As}(r)e^{i[l+(1-s)/2]\phi} \\ \chi_l^{Bs}(r)e^{i[l+(1+s)/2]\phi} \end{pmatrix}, \tag{A1}$$

where $s=\pm$; obviously $s=\pm 1$ when occurring in a phase. As a result, the matrix eigenvalue problem is equivalent to the following set of equations involving the vector components:

$$-i\hbar v_F \partial_r \chi_l^{B+} - i\hbar v_F (l+1)\frac{\chi_l^{B+}}{r} = E\chi_l^{A+} - i\hbar v_F \partial_r \chi_l^{A+} + i\hbar v_F l \frac{\chi_l^{A+}}{r} = E\chi_l^{B+}, \tag{A2}$$

where we considered only the case for $s=+$ (the $s=-$ case can be treated in a similar way).

We are interested in solutions with $E=0$ (the so-called midgap solutions), in which case the set of Eq. (A2) reduces to

$$\partial_r \chi_l^{B+} + \frac{(l+1)}{r}\chi_l^{B+} = 0,$$

$$\partial_r \chi_l^{A+} - \frac{l}{r}\chi_l^{A+} = 0. \tag{A3}$$

The solutions of these equations are

$$\chi_l^{B+}(r) = \chi_l^{B+}(R)\left(\frac{r}{R}\right)^{-l-1},$$

$$\chi_l^{A+}(r) = \chi_l^{A+}(R)\left(\frac{r}{R}\right)^{l}. \tag{A4}$$

The boundary condition is that of a zigzag graphene edge that ends always on a site of the same lattice, i.e., the condition

$$\chi_l^{B+}(R) = 0 \tag{A5}$$

forces the $B+$ component to vanish everywhere on the B sublattice, yielding the final form

$$\begin{pmatrix} \psi_l^{A+} \\ \psi_l^{B+} \end{pmatrix} = \begin{pmatrix} \chi_l^{A+}(R)\left(\frac{r}{R}\right)^{l} e^{il\phi} \\ 0 \end{pmatrix}. \tag{A6}$$

The normalization constant $\chi_l^{A+}(R)$ is easily calculated and is given in Eq. (4).

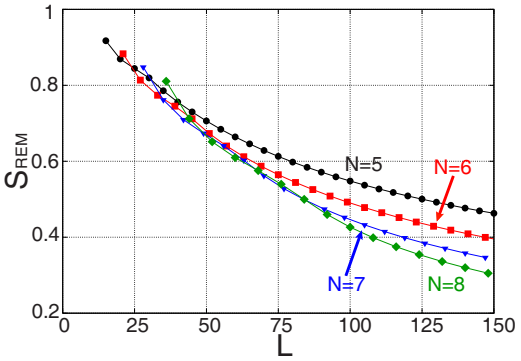

FIG. 12. (Color online) Overlaps of the parameter-free trial REM states [i.e., for $\alpha=1$, see Eq. (16)] with the EXD ones, as a function of total angular momentum L.

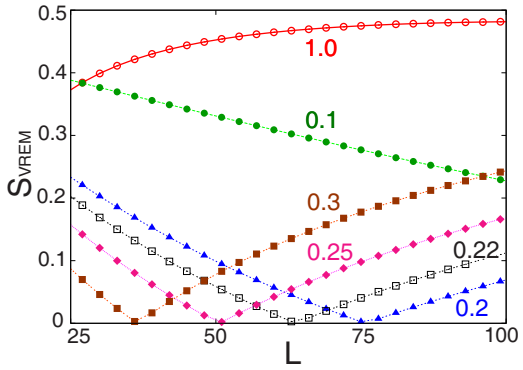

FIG. 13. (Color online) Overlaps of the variational REM states with the EXD *first-excited* states for selected values of the variational parameter α [see Eq. (18)] as a function of total angular momentum L. The drops toward zero determine the optimal α's for given L's. For $\alpha=1$ (top curve), no such drop to zero occurs.

APPENDIX B: THE PARAMETER-FREE REM ($\alpha=1$)

As mentioned in Sec. V C, the overlaps $\mathcal{S}_{\mathrm{REM}} \equiv \langle \Phi_{N,L}^{\mathrm{EXD}} | \Phi_{N,L}^{\mathrm{REM}} \rangle$ between the parameter-free REM waves function in the GD-LLL and the EXD ones behave in an unsatisfactory way, i.e., they decrease as L increases. The precise behavior of $\mathcal{S}_{\mathrm{REM}}$ is displayed in Fig. 12, and it contrasts with that of the variational REM, $\mathcal{S}_{\mathrm{VREM}}$, displayed in Fig. 6.

The degradation of the $\mathcal{S}_{\mathrm{REM}}$ reflects the fact that progressively the overlap of the REM wave function with the *excited* EXD states increases with increasing L. On the other hand, the optimized values of α correspond to variational REM trial functions that have practically zero overlap with these excited EXD ones. We have found that such optimal α values can be found for all studied values of N and L. This is illustrated in Fig. 13, where the overlaps of the VREM with the first-excited EXD state dip toward zero at the optimal α values.

APPENDIX C: SINGLE-PARTICLE DENSITY

We give here the expression for calculating the single-particle density $\rho(z)$ for a single many-body state $\Phi_L[z] = \Sigma_I C_L^I \Psi_L^I[z]$, where the basis wave functions Ψ_L^I are the Slater determinants defined by Eq. (20). Specifically, one has

$$\rho(z) = \langle \Phi_L | \sum_{k=1}^{N} \delta(z - z_k) | \Phi_L \rangle = \sum_I \sum_J C_L^{I*} C_L^J \langle \Psi_L^I | \sum_{k=1}^{N} \delta(z - z_k) \times | \Psi_L^J \rangle = \sum_I |C_L^I|^2 \langle \Psi_L^I | \sum_{k=1}^{N} \delta(z - z_k) | \Psi_L^I \rangle = \sum_I |C_L^I|^2 \sum_{k=1}^{N} \psi_{l_k^I}^*(z) \psi_{l_k^I}(z) = \sum_I |C_L^I|^2 \sum_{k=1}^{N} \frac{l_k^I + 1}{\pi R^2} \left(\frac{r}{R} \right)^{2 l_k^I}, \tag{C1}$$

where the edge states ψ's are given by Eq. (6) and l_k^I denotes the single-particle angular momenta associated with the Slater determinant Ψ_L^I; naturally $L = \Sigma_{k=1}^N l_k^I$. The single-particle density operator connects in principle Slater determinants that differ at most in one orbital. However, in the LLL, the conservation of the total angular momentum implies that there are no pair of Slater determinants in the linear superposition of Φ_L that differ precisely by one single orbital; thus one sets $J=I$ when deriving Eq. (C1).

APPENDIX D: SINGLE-PARTICLE DENSITY FOR A SUPERPOSITION OF TWO WAVE FUNCTIONS

In Sec. VI we discussed how the disruptions in the zigzag boundary conditions create crystal-field effects that pin the rotating-electron molecule. The effect of this pinning is described through the linear superposition of two many-body wave functions (EXD and/or REM) with magic good-total angular momenta L and M, namely, through a wave function Φ^{PIN} such that

$$\Phi^{\mathrm{PIN}} = \frac{1}{\sqrt{2}} (\Phi_L \pm \Phi_M), \tag{D1}$$

where we have dropped the subscript N and superscripts "EXD" or "REM" from the $\Phi_{L(M)}$'s on the right-hand side.

The $\Phi_{L(M)}$'s are known through their expansions over Slater determinants (see Sec. IV), i.e,

$$\Phi_L = \sum_I C_L^I \Psi_L^I, \quad \Phi_M = \sum_J C_M^J \Psi_M^J, \tag{D2}$$

and the Slater determinants Ψ_L^I and Ψ_M^J are built out of single-particle states having individual angular momenta l_i^I and m_j^J such that $\Sigma_{k=1}^N l_k^I = L$ and $\Sigma_{k=1}^N m_k^J = M$. Using the operator $\hat{\rho}$ defined by the first line of Eq. (C1), the single-particle density is given by

$$\rho^{\mathrm{PIN}}(z) = \langle \Phi^{\mathrm{PIN}} | \hat{\rho} | \Phi^{\mathrm{PIN}} \rangle = \frac{1}{2} (\langle \Phi_L | \hat{\rho} | \Phi_L \rangle + \langle \Phi_M | \hat{\rho} | \Phi_M \rangle \pm \langle \Phi_L | \hat{\rho} | \Phi_M \rangle \pm \langle \Phi_M | \hat{\rho} | \Phi_L \rangle). \tag{D3}$$

The diagonal terms $\langle \Phi_L | \hat{\rho} | \Phi_L \rangle$ and $\langle \Phi_M | \hat{\rho} | \Phi_M \rangle$ are given by Eq. (C1). Since $\hat{\rho}$ is a one-body operator, the cross terms connect Slater determinants that differ precisely by one of

orbital;[43] we denote by l_p^I and m_q^J the corresponding pair of indices. By applying the Slater rules described in Ref. 43 (including bringing the two determinants into "maximum coincidence"), one finds

$$\rho^{\mathrm{PIN}}(z) = \sum_I |C_L^I|^2 \sum_{k=1}^{N} \frac{(l_k^I+1)}{\pi R^2}\left(\frac{r}{R}\right)^{2l_k^I} + \sum_J |C_M^J|^2 \sum_{k=1}^{N} \frac{(m_k^J+1)}{\pi R^2}\left(\frac{r}{R}\right)^{2m_k^J} \pm \sum_{I,J} C_L^{I*} C_M^J \sigma(L,I,p;M,J,q) \frac{\sqrt{(l_p^I+1)(m_q^J+1)}}{\pi R^2}\left(\frac{r}{R}\right)^{l_p^I+m_q^J} e^{-i\phi(l_p^I-m_q^J)} \pm \sum_{I,J} C_M^{I*} C_L^J \sigma(M,I,q;L,J,p) \frac{\sqrt{(m_q^I+1)(l_p^J+1)}}{\pi R^2}\left(\frac{r}{R}\right)^{m_q^I+l_p^J} e^{-i\phi(m_q^I-l_p^J)}, \tag{D4}$$

where $\sigma(L,I,p;M,J,q)=\pm 1$ depending on the even or odd number of exchanges of two rows (or columns) needed to bring the two determinants into maximum coincidence.

APPENDIX E: TWO-PARTICLE CONDITIONAL PROBABILITY DISTRIBUTION

For the conditional probability density [see Eq. (28)], one has

$$P(z,z_0) = \sum_I \sum_J C_L^{*I} C_L^J \langle \Psi_L^I | \hat{T} | \Psi_L^J \rangle, \tag{E1}$$

where the operator $\hat{T}$ is symmetrized,

$$\hat{T} = \sum_{i<j} \delta(z-z_i)\delta(z_0-z_j) + \delta(z-z_j)\delta(z_0-z_i). \tag{E2}$$

The matrix elements of $\hat{T}$ between the two Slater determinants Ψ_L^I and Ψ_L^J are calculated according to the Slater rules for a two-body operator.[43]

APPENDIX F: MORE ON COMPOSITE FERMIONS

There is no reason to *a priori* restrict the Slater determinants $\Psi_{L^*}^{\mathrm{IPM}}$ to a certain form.[51] Following Ref. 51, we will restrict the noninteracting L^* to the range $-L_0 \le L^* \le L_0$, and we will assume that the Slater determinants $\Psi_{L^*}^{\mathrm{IPM}}$ are the so-called compact ones. Let N_n denote the number of electrons in the nth Landau level (LL) with $\Sigma_{n=0}^t N_n = N$; t is the index of the highest occupied LL and all the lower LL's with $n \le t$ are assumed to be occupied. The compact determinants are defined as those in which the N_n electrons occupy contiguously the single-particle orbitals $[\psi_{p,l}^{\mathrm{DF}}(z)]$ of each nth LL $[p+(|l|-l)/2=n]$ with the lowest angular momenta, $l=-n, -n+1, \ldots, -n+N_n-1$. The compact Slater determinants are usually denoted as $[N_0,N_1,\ldots,N_t]$ and the corresponding total angular momenta are given by $L^*=(1/2)\Sigma_{s=0}^t N_s(N_s-2s-1)$.

For the CF theory, the magic angular momenta can be determined by Eq. (31) if one knows the noninteracting L^*'s. For $N=6$, the CF magic L's in any interval $1/(2m-1) \ge \nu \ge 1/(2m+1)$ $[15(2m-1) \le L \le 15(2m+1)]$, $m=1,2,3,4,\ldots$, can be found by adding $2mL_0=30m$ units of angular momentum to each of the L^*'s. To obtain the noninteracting L^*'s, one needs first to construct[51] the compact Slater determinants. The compact determinants and the corresponding noninteracting L^*'s are listed in Table II.

There are nine different values of L^*'s, and thus the CF theory for $N=6$ predicts that there are always eight magic-numbers in any interval $15(2m-1) \le L < 15(2m+1)$ between two consecutive JL angular momenta $15(2m-1)$ and $15(2m+1)$, $m=1,2,3,\ldots$. For example, using Table II and Eq. (31), the CF magic numbers for $N=6$ in the interval $15 \le L < 45$ $(m=1)$ are found to be the following eight:

$$15,\ 21,\ 25,\ 27,\ 30,\ 33,\ 35,\ 39. \tag{F1}$$

In the interval $45 \le L < 75$ $(m=2)$, the CF magic numbers are

$$45,\ 51,\ 55,\ 57,\ 60,\ 63,\ 65,\ 69. \tag{F2}$$

TABLE II. Compact noninteracting Slater determinants and associated angular momenta L^* for $N=6$ electrons according to the CF prescription. Both $L^*=-3$ and $L^*=3$ are associated with two compact states each, the one with lowest energy being the preferred one.

Compact state $[N_0,N_1,\ldots,N_t]$	L^*
[1,1,1,1,1,1]	−15
[2,1,1,1,1]	−9
[2,2,1,1]	−5
[3,1,1,1]	−3
[2,2,2]	−3
[3,2,1]	0
[4,1,1]	3
[3,3]	3
[4,2]	5
[5,1]	9
[6]	15

[1] D. C. Tsui, H. L. Stormer, and A. C. Gossard, Phys. Rev. Lett. **48**, 1559 (1982).
[2] R. B. Laughlin, Phys. Rev. Lett. **50**, 1395 (1983).
[3] F. D. M. Haldane, Phys. Rev. Lett. **51**, 605 (1983).
[4] B. I. Halperin, Phys. Rev. Lett. **52**, 1583 (1984).
[5] J. K. Jain, Phys. Rev. Lett. **63**, 199 (1989).
[6] R. B. Laughlin, Rev. Mod. Phys. **71**, 863 (1999), and references therein.
[7] J. K. Jain, *Composite Fermions* (Cambridge University Press, Cambridge, 2007), and references therein.
[8] C. Yannouleas and U. Landman, Phys. Rev. B **66**, 115315 (2002).
[9] C. Yannouleas and U. Landman, Phys. Rev. B **68**, 035326 (2003).
[10] C. Yannouleas and U. Landman, Phys. Rev. B **70**, 235319 (2004).
[11] C. Yannouleas and U. Landman, Rep. Prog. Phys. **70**, 2067 (2007).
[12] C. C. Chang, G. S. Jeon, and J. K. Jain, Phys. Rev. Lett. **94**, 016809 (2005).
[13] C. C. Chang, C. Töke, G. S. Jeon, and J. K. Jain, Phys. Rev. B **73**, 155323 (2006).
[14] N. K. Wilkin and J. M. F. Gunn, Phys. Rev. Lett. **84**, 6 (2000).
[15] N. R. Cooper, N. K. Wilkin, and J. M. F. Gunn, Phys. Rev. Lett. **87**, 120405 (2001).
[16] M. Popp, B. Paredes, and J. I. Cirac, Phys. Rev. A **70**, 053612 (2004).
[17] C. C. Chang, N. Regnault, T. Jolicoeur, and J. K. Jain, Phys. Rev. A **72**, 013611 (2005).
[18] N. Barberán, M. Lewenstein, K. Osterloh, and D. Dagnino, Phys. Rev. A **73**, 063623 (2006).
[19] L. O. Baksmaty, C. Yannouleas, and U. Landman, Phys. Rev. A **75**, 023620 (2007).
[20] K. S. Novoselov, A. K. Geim, S. V. Morozov, D. Jiang, Y. Zhang, S. V. Dubonos, I. V. Grigorieva, and A. A. Firsov, Science **306**, 666 (2004).
[21] C. Berger, Z. M. Song, T. B. Li, X. B. Li, A. Y. Ogbazghi, R. Feng, Z. T. Dai, A. N. Marchenkov, E. H. Conrad, P. N. First, and W. A. de Heer, J. Phys. Chem. B **108**, 19912 (2004).
[22] K. S. Novoselov, A. K. Geim, S. V. Morozov, D. Jiang, M. I. Katsnelson, I. V. Grigorieva, S. V. Dubonos, and A. A. Firsov, Nature (London) **438**, 197 (2005).
[23] Y. B. Zhang, Y. W. Tan, H. L. Stormer, and P. Kim, Nature (London) **438**, 201 (2005).
[24] A. K. Geim and K. S. Novoselov, Nature Mater. **6**, 183 (2007).
[25] J. Kedzierski, Hsu Pei-Lan, P. Healey, P. W. Wyatt, C. L. Keast, M. Sprinkle, C. Berger, and W. A. de Heer, IEEE Trans. Electron Devices **55**, 2078 (2008).
[26] A. H. Castro Neto, F. Guinea, N. M. R. Peres, K. S. Novoselev, and A. K. Geim, Rev. Mod. Phys. **81**, 109 (2009).
[27] M. I. Katsnelson, K. S. Novoselov, and A. K. Geim, Nat. Phys. **2**, 620 (2006).
[28] O. Klein, Z. Phys. **53**, 157 (1929).
[29] N. Dombey and A. Calogeracos, Contemp. Phys. **40**, 313 (1999).
[30] Z. Chen, Y. Lin, M. Rooks, and P. Avouris, Physica E (Amsterdam) **40**, 228 (2007).
[31] M. Y. Han, B. Ozyilmaz, Y. Zhang, and P. Kim, Phys. Rev. Lett. **98**, 206805 (2007).
[32] X. Li, X. Wang, L. Zhang, S. Lee, and H. Dai, Science **319**, 1229 (2008).
[33] C. Stampfer, J. Guttinger, F. Molitor, D. Graf, T. Ihn, and K. Esslin, Appl. Phys. Lett. **92**, 012102 (2008).
[34] S. Schnez, F. Molitor, C. Stampfer, J. Güttinger, I. Shorubalko, T. Ihn, and K. Ensslin, arXiv:0807.2710 (unpublished).
[35] S. Schnez, K. Ensslin, M. Sigrist, and T. Ihn, Phys. Rev. B **78**, 195427 (2008).
[36] M. Fujita, K. Wakabayashi, K. Nakada, and K. Kusakabe, J. Phys. Soc. Jpn. **65**, 1920 (1996).
[37] K. Nakada, M. Fujita, G. Dresselhaus, and M. S. Dresselhaus, Phys. Rev. B **54**, 17954 (1996).
[38] B. Wunsch, T. Stauber, and F. Guinea, Phys. Rev. B **77**, 035316 (2008).
[39] T. Ando, J. Phys. Soc. Jpn. **74**, 777 (2005).
[40] There is also a mirror LLL for $l \leq 0$ in analogy with the effect of reversing the direction of the magnetic field in semiconductor QDs.
[41] Symmetry restoration techniques as a second step beyond the broken-symmetry mean-field level (and in particular in relation to the three-dimensional total angular momentum) were introduced in nuclear physics in R. E. Peierls and J. Yoccoz, Proc. Phys. Soc., London, Sect. A **70**, 381 (1957); For a review of such methods in newly emerging areas of condensed-matter finite systems (specifically in the case of electrons confined in two-dimensional quantum dots and of trapped ultracold bosonic clouds), see Ref. 11, and references therein, as well as I. Romanovsky, C. Yannouleas, and U. Landman, Phys. Rev. A **78**, 011606(R) (2008).
[42] Due to the length of the expressions involved for $N > 3$, one needs to use an algebraic software language like MATHEMATICA; see S. Wolfram, *Mathematica: A System for Doing Mathematics by Computer* (Addison-Wesley, Reading, MA, 1991).
[43] A. Szabo and N. S. Ostlund, *Modern Quantum Chemistry* (McGraw-Hill, New York, 1989), Chap. 2.3.3.
[44] E. W. Weisstein, *CRC Concise Encyclopedia of Mathematics*, 2nd ed. (CRC Press, Boca Raton, FL, 2003).
[45] P. A. Maksym, H. Imamura, G. P. Mallon, and H. Aoki, J. Phys.: Condens. Matter **12**, R299 (2000).
[46] C. G. Darwin, Proc. Cambridge Philos. Soc. **27**, 86 (1930); V. Fock, Z. Phys. **47**, 446 (1928).
[47] J. K. Jain and R. K. Kamilla, in *Composite Fermions: A Unified View of the Quantum Hall Regime*, edited by O. Heinonen (World Scientific, Singapore, 1998), p. 1.
[48] G. S. Jeon, C. C. Chang, and J. K. Jain, Eur. Phys. J. B **55**, 271 (2007).
[49] A. R. Akhmerov and C. W. J. Beenakker, Phys. Rev. B **77**, 085423 (2008).
[50] While for a graphene quantum dot in the *absence* of a magnetic field only the edge states have zero energy, the development of a bulklike (volume) Landau spectrum (with one of the Landau levels having zero energy) for dots under the *influence* of a magnetic field has been studied in Ref. 35 and by P. Recher, J. Nilsson, G. Burkard, and B. Trauzettel, arXiv:0810.0419 (unpublished). It has been found that bulklike Landau levels (and thus zero-energy volume states) develop only in the case of $R/\Lambda_{\mathcal{B}} \gg 1$, where R is the radius of the dot and $\Lambda_{\mathcal{B}}$ is the magnetic length (see Sec. II A). For $\mathcal{B}=0$ (our case), $R \to \infty$ in order to satisfy this condition, which means that zero-energy volume states do not occur for a zero magnetic field even for very large dots.
[51] J. K. Jain and T. Kawamura, Europhys. Lett. **29**, 321 (1995).